

# Numerical and Experimental Study of a Covert-Inspired Passively Deployable Flap for Aerodynamic Lift Enhancement

Ahmed K. Othman <sup>a\*</sup>, Nirmal J. Nair <sup>b†</sup>, Anushka Sandeep <sup>b‡</sup>, Andres Goza <sup>b§</sup>, and Aimy Wissa<sup>a¶</sup>

<sup>a</sup> Princeton University, Princeton, New Jersey, 08544

<sup>b</sup> University of Illinois at Urbana-Champaign, Urbana, Illinois, 61801

Bio-inspired flow control techniques have the potential to overcome the operational and environmental limitations of traditional flow control techniques. One of those bio-inspired flow control techniques is covert-inspired flaps. Covert bird feathers act as aeroelastic high-lift devices capable of controlling separation and mitigating stall. This study investigates the performance characteristics of a covert-inspired passive flow control technique using numerical simulations and experiments at two significantly different Reynolds numbers (Re), Re = 1000 and  $Re = 2 \times 10^5$ , respectively. The covert feathers are modeled as passively deployable, torsionally hinged flaps on the upper surface of a NACA2414 airfoil. We perform a systematic parametric study, where we varied the flap hinge location, hinge stiffness, and rotational inertia of the flap. Results from this study quantify the effects of the hinge stiffness and flap inertia on lift improvements and flap dynamics across Reynolds number. A key feature of this study is the assessment of critical similarities and differences in the physics of the covert-inspired flap FSI system across these different Reynolds numbers. We perform this comparison by measuring and contrasting the flow and flap dynamics as well as the average and instantaneous lift force.

# **Nomenclature**

$\alpha$	=	angle of attack
β	=	flap deployment angle
$\frac{\beta}{\beta}$	=	mean flap deployment angle
c	=	airfoil chord length
$C_l$	=	coefficient of lift
$\frac{C_l}{\Delta \overline{C}_l}$	=	percentage change in mean lift relative to baseline airfoil
f	=	surface stress on body
Fr	=	Froude number
$\boldsymbol{g}$	=	gravitational field
g	=	reference acceleration due to gravity
Γ	=	set of bodies
$\Gamma_a, \Gamma_f$	=	bodies of airfoil and flap
$i_{eta}, I_{eta}$	=	dimensionless and dimensional flap moment of inertia
$k_{\beta}, K_{\beta}$	=	dimensionless and dimensional stiffness of torsional spring
$l_{\beta}, L_{\beta}$	=	dimensionless and dimensional chordwise flap location
$l_f$	=	length of the flap
ν	=	kinematic viscosity
p, P	=	dimensionless and dimensional pressure field
$P_{\infty}$	=	freestream pressure
$ ho_f$	=	fluid density
Re	=	Reynolds number
St	=	Strouhal number

<sup>\*</sup>Graduate Research Assistant, Department of Mechanical and Aerospace Engineering, AIAA Student Member

<sup>†</sup>Graduate Research Assistant, Department of Aerospace Engineering, AIAA Student Member

<sup>&</sup>lt;sup>‡</sup>Undergraduate Research Assistant, Department of Mechanical Science and Engineering

<sup>§</sup> Assistant Professor, Department of Aerospace Engineering, AIAA Member

<sup>¶</sup>Assistant Professor, Department of Mechanical and Aerospace Engineering, AIAA Member

t = time

T = time period of steady limit cycle oscillations (LCO)

u = fluid velocity  $U_{\infty}$  = freestream velocity

 $\chi, \chi_a, \chi_f$  = Lagrangian coordinate of body, airfoil and flap

 $\chi_f^0, \chi_f^{cg}$  = flap hinge location and center of gravity

 $\Omega$  = flow domain

### I. Introduction

Stall in the context of aerodynamics is used to refer to a significant drop in the lift generated by a wing or an airfoil as the angle of the attack increases beyond a certain angle referred to as the critical angle of attack [1]. It occurs as a result of the global flow separation happening on the upper surface of the wing due to a combination of the viscous effects and adverse pressure gradient at high angles of attack [2]. Multiple experimental and numerical studies such as the ones done by Selig in 1999 and Abbott & von Doenhoff in 1958 have analyzed the effect of stall for multiple airfoils at several Reynolds numbers (Re) [3, 4]. These studies show that the stall behavior, especially the critical angle of attack of an airfoil, is a function of the airfoil geometry and the chord Reynolds number [5]. At low Reynolds numbers,  $Re \le 20000$ , the flow is laminar; therefore, stall occurs as a result of the burst of the laminar separation bubble, resulting in a laminar separation zone that causes stall. For intermediate Reynolds numbers, (30000  $\le Re \le 300000$ ), stall occurs due to a combination of the effects of the burst of the laminar separation bubble along with the turbulence transition effects and the formation of convective vortical eddies leading to flow unsteadiness and stall. At both Reynolds number regimes, stall limits the flight envelope for an aircraft by limiting its maximum lift production and its operational angles of attack [2].

Multiple flow control techniques have been implemented to mitigate the effects of stall in order to expand the possible flight envelop of an aircraft. Vortex generators, leading-edge slats, and wall jets are examples of traditional flow control techniques that are used to delay and mitigate stall effects. Moreover, control methodologies have leveraged recent advances in bio-inspired flow control. Leading-edge serrations, slotted wingtips, and alula-inspired leading-edge devices are all examples of bio-inspired flow control techniques that aid with mitigating stall effects. Bio-inspired flow control techniques provide an alternative approach that has the potential to overcome the current operational and environmental challenges of traditional flow control techniques [6–8].

We focus here on a bio-inspired flow control device inspired by the covert feathers in birds. The coverts are contour feathers that cover both the upper and lower sides of bird wings. There are multiple rows of covert feathers on both wing sides, as shown in Fig. 1a. Coverts are noticed to deploy during high-angle-of-attack maneuvers such as perching, take-off, and landing[9]. The covert feathers consist mainly of a central shaft and two laterally attached vanes (Fig. 1b). The shaft is divided into two parts: the rachis which is the long tubular extension of the shaft above the skin and the calamus which is the root of the shaft that's connected to the skin. Two parameters affect the flexibility of the coverts feather and their response to the flow, namely the shaft stiffness determined by the material properties and the shaft moment of inertia defined by the geometry. [10, 11]. Thus, the stiffness and inertial properties of a covert feather or a covert-inspired flow control device are critical parameters that control its deployment dynamics and conditions.

Carruthers et al. [9] observed the covert feather deployment during flight, and referred to the coverts as nature's high lift aeroelastic devices that mitigate undesirable, unsteady flow conditions [9]. The coverts were found to deploy during high-angle-of-attack maneuvers and in gusty conditions. Bio-inspired studies have borrowed from these insights to produce covert-inspired flaps that increase post-stall lift production and expand the flight envelope. Rigid metal flaps, feathered flaps, and elastic hair-like flaps are all examples of covert-inspired flaps that have been placed at various wing locations to augment aerodynamic performance [12–15]. Despite the different structural forms of the covert-inspired flaps, most studies confirmed that the flaps improve lift, especially at post-stall angles of attack. For example, Duan and Wissa [16] showed that static covert-inspired flaps placed between 40 and 80 percent of the chord on the upper surface of the wing can improve post-stall lift by up to 23% at  $Re = 2 \times 10^5$ . In another study, Meyer et al. [17] tested freely hinged (i.e., hinged with zero stiffness) aluminum flaps on HQ17 and HQ41 airfoils at  $1 \times 10^6 \le Re \le 2 \times 10^6$ . The author concluded that if the flap is attached near the leading edge, it will disturb the laminar flow usually observed in this region, leading to earlier transition and significant increase in drag. Therefore, the study recommends that the trailing edge of the movable flap should be located slightly upstream of the trailing edge of the airfoil to respond properly to flow separation. At the lower-Reynolds-number regime, a study by Rosti et al. [15] at Re = 2000 showed that a single flap hinged on the suction side of an NACA 0020, located between 60 and 70 percent of the wing chord on the upper

surface, results in the best improvements in lift and lift-to-drag ratio at a post-stall angle  $\alpha = 20^{\circ}$  [15].



- (a) Upper wing coverts on a heron wing[18]
- (b) Structure of heron's upper and under wing coverts [19]

Fig. 1 Coverts on the upper surface of a heron wing where LC is lesser coverts, MC is median coverts, and GC is greater coverts (left) and the upper and under wing covert feathers structure (right). (Photo Credit: (left) by TheOtherKiv/Pixabay and (right) The Feather Atlas)

While the overall effects of covert-inspired flaps on performance across different studies may seem similar, there is a lack of understanding about the physical mechanisms that allow such lift improvement, especially across different Reynolds numbers. Understanding these mechanisms can guide the design of flow control devices for both low- and intermediate-Reynolds-number flows. Such Reynolds number regimes are critical for small unmanned aerial vehicles (UAVs) that operate at the higher end of  $Re \sim O(10^5)$  and micro-air vehicles (MAVs) that maneuver at lower Reynolds numbers,  $Re \sim O(10^3-10^4)$ . Across this Re range, key variations in the flow behavior are well known. For instance, low Re aerodynamic flows are characterized by significant regions of laminar flow but prone to early flow separation and vortex shedding due to the inability of the lower momentum flow to overcome the adverse pressure gradient aft of the point of maximum thickness. On the other hand, flow transition and turbulence become more prevalent as Reynolds number is increased. A detailed comparison study of the variations in flap dynamics and how they affect aerodynamic performance for Reynolds numbers spanning three orders of magnitude can provide crucial insights for designing covert-inspired flow control techniques across various flight regimes.

The overall goal of this work is to investigate and compare the aerodynamic effects of covert-inspired flaps across a wide range of Reynolds numbers. Such a comparison across Reynolds numbers can be performed either numerically or experimentally. Numerical simulations of laminar flows at  $Re \sim O(10^3)$  can be performed at very small computational costs as compared to higher-Reynolds-number flows. These simulations can also be performed more routinely than conducting wind tunnel experiments. On the other hand, experiments can reveal true physical insights of the covert-inspired flow control technique. Experimental investigations are particularly critical at the upper end of the Reynolds number regime, where fully resolved numerical models are prohibitively costly. Therefore, we adopt here a hybrid approach of numerical simulations at low Reynolds numbers and experiments at high Reynolds numbers, towards informing design parameters across a range of flow inertia. Moreover, if sufficient similarities in the flap dynamics and flow phenomena are observed across Reynolds numbers, then the numerical simulations can be effectively used to design the experimental setup at high Reynolds numbers (with re-scaling of relevant variables informed by comparisons such as the one performed in this study).

In this work, we study the performance characteristics of a covert-inspired passive flow control technique using numerical simulations and experiments at two significantly different Reynolds numbers of Re = 1000 and  $Re = 2 \times 10^5$ , respectively. The covert feathers are modeled as a passively deployable, torsionally hinged rigid flap on the upper surface of a NACA2414 airfoil. The low Re = 1000 flow past the airfoil-flap system is studied via two-dimensional (2D) high-fidelity numerical simulations in an immersed boundary framework. On the other hand, the higher  $Re = 2 \times 10^5$  case is studied experimentally through wind tunnel tests. For both the cases, the airfoil is affixed at a large post-stall angle of attack of  $20^\circ$  where significant flow separation and vortex shedding are observed. We perform a systematic

parametric study, where we vary the flap hinge location, hinge stiffness, and rotational inertia of the flap. Results of this study inform the key similarities and differences in the flap dynamics across Reynolds number, and how they play a role in providing aerodynamic benefits.

The remainder of the paper is organized as follows: Section II present the common problem parameters and details the numerical and experimental methods. Section III presents the results for the averaged and instantaneous lift forces and flap deflections and discusses the similarities and difference across Re, and Section IV includes conclusions and recommendation for future work.

### II. Problem Parameters and Methods

### A. Problem Overview and Parameters

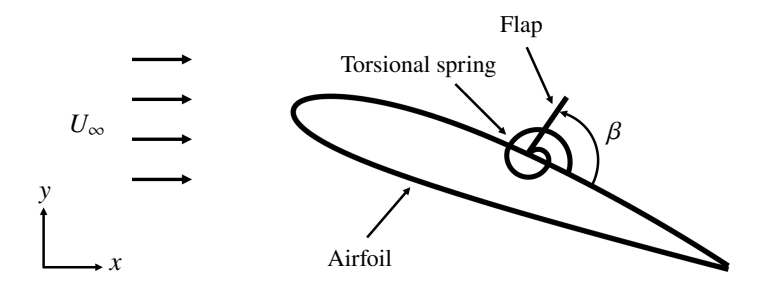


Fig. 2 Schematic of the system of passively deployable flap on an airfoil

In this work, we model the covert feathers as a passively deployable, torsionally mounted rigid flap on the upper surface of a stationary NACA2414 airfoil as shown in Fig. 2. This airfoil was selected because it has been well characterized in wind tunnel tests across various Reynolds number and it is suitable for small-scale UAVs. The Reynolds number based on the chord length is set to Re = 1000 and  $Re = 2 \times 10^5$  for the numerical simulations and experiments, respectively. Fig. 3 displays the  $C_l$  v/s  $\alpha$  plot for the flap-less NACA2414 airfoil at these two Re. Clearly, for  $Re = 2 \times 10^5$ ,  $\alpha = 20^\circ$  corresponds to a post-stall angle of attack due to the sharp decline in  $C_l$  after  $\alpha = 16^\circ$ . On the other hand, for Re = 1000, the stall angle is not discernible since the lift continues to increase with increasing  $\alpha$ . Therefore, to identify the stall angle, we have also shown the amplitude of fluctuations in  $C_l$  denoted by the gray shaded region. These (limit cycle) oscillations occur due to flow separation on the upper surface of the airfoil and ensuing periodic vortex shedding. Notable flow separation induced fluctuations can be observed starting from  $\alpha = 10^\circ$  with significant fluctuations at  $20^\circ$ . Therefore,  $\alpha = 20^\circ$  corresponds to a post-stall angle for Re = 1000 as well.

For the simulations and experiments, the chord length of the airfoil is denoted by c and the length of the flap is fixed at 0.15c. Both the experiments and simulations are simulated under gravity with Froude number  $(Fr = U_{\infty}/\sqrt{gc})$  of 23.96. The varying flap and hinge parameters in this study are the moment of inertia of the flap,  $I_{\beta}$ , the stiffness of the torsional spring representing the hinge,  $K_{\beta}$  and the chordwise distance of the flap from the leading edge,  $L_{\beta}$ . These parameters are non-dimensionalized as,

$$i_{\beta} = \frac{I_{\beta}}{\rho_f c^4}, \qquad k_{\beta} = \frac{K_{\beta}}{\rho_f U_{\infty}^2 c^2}, \qquad l_{\beta} = \frac{L_{\beta}}{c}$$
 (1)

Here, the reference length scale is the airfoil chord c, velocity scale is the freestream velocity  $U_{\infty}$  and reference density is the fluid density  $\rho_f$ ;  $i_{\beta}$ ,  $k_{\beta}$  and  $l_{\beta}$  are the non-dimensional counterparts of  $I_{\beta}$ ,  $K_{\beta}$  and  $L_{\beta}$ . In the manuscript, the parameter  $l_{\beta}$  is reported as percentage of chord length from the leading edge. The length and locations of the flap were specified based on several design parameters in the literature [14, 16, 20, 21]. All the fixed and varying parameters for the numerical simulations and experiments are reported in Table 1. From Table 1, it is clear that the only key different parameter is Reynolds number, allowing us to investigate its effects on the flap dynamics and the flap-induced aerodynamic improvements.

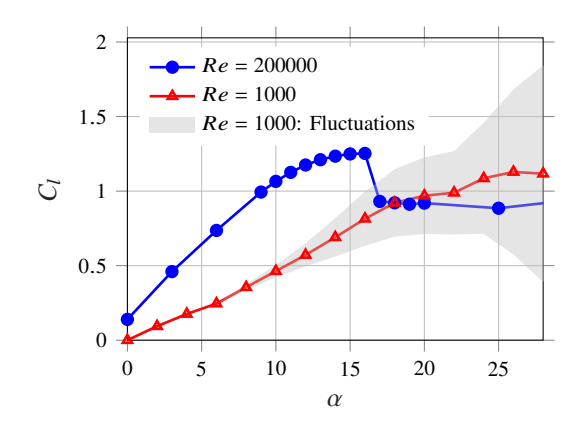


Fig. 3  $C_l$  v/s  $\alpha$  for  $Re = 2 \times 10^5$  and Re = 1000. Gray shaded region denotes the amplitude in fluctuations in  $C_l$  at Re = 1000.

	Parameters	Values	
Fixed parameters	Re	Experimental	Numerical
	Ke	200000	1000
	Airfoil	NACA2414	
	Angle of attack	20°	
	Flap length	0.15	
	Fr	23.96	
Varying parameters	Flap location $(l_{\beta})$	{20, 50, 70}%	
	Stiffness of hinge $(k_{\beta})$	{0.0001, 0.0005, 0.001}	
	Flap moment of inertia $(i_{\beta})$	{0.0012, 0.012}	

Table 1 List of fixed and varying parameters for experiments and numerical simulations.

### **B.** Numerical methodology

The simulations are performed using the strongly-coupled immersed boundary method of Goza and Colonius [22] which has been implemented and verified on problems involving torsionally mounted flaps [21]. This method solves the following dimensionless governing equations,

$$\frac{\partial \mathbf{u}}{\partial t} + \mathbf{u} \cdot \nabla \mathbf{u} = -\nabla p + \frac{1}{Re} \nabla^2 \mathbf{u} + \int_{\Gamma} f(\chi(s,t)) \delta(\chi(s,t) - \mathbf{x}) ds + \frac{1}{Fr^2} \mathbf{g}$$
 (2)

$$\nabla \cdot \boldsymbol{u} = 0 \tag{3}$$

$$i_{\beta} \frac{\partial^{2} \beta}{\partial t^{2}} + k_{\beta} \beta = -\int_{\Gamma_{f}} (\chi_{f} - \chi_{f}^{0}) \times f(\chi_{f}) d\chi_{f} + \frac{3i_{\beta}}{l_{f}^{2} F r^{2}} (\chi_{f}^{cg} - \chi_{f}^{0}) \times \mathbf{g}$$

$$\tag{4}$$

$$\int_{\Omega} \mathbf{u}(\mathbf{x})\delta(\mathbf{x} - \mathbf{\chi}_a)d\mathbf{x} = 0 \tag{5}$$

$$\int_{\Omega} \boldsymbol{u}(\boldsymbol{x})\delta(\boldsymbol{x} - \boldsymbol{\chi}_f)d\boldsymbol{x} = \frac{\partial \beta}{\partial t}\hat{\boldsymbol{e}}^i \times (\boldsymbol{\chi}_f - \boldsymbol{\chi}_f^0)$$
 (6)

In the above, x denotes the Eulerian coordinate representing a position in the fluid domain  $\Omega$  and  $\chi(s,t)$  denotes the Lagrangian coordinate attached to the bodies (airfoil and flap) in the set  $\Gamma$ , the surface of which is parameterized by the variable s. These variables, x,  $\chi$  and s were nondimensionalized by c; velocity u was nondimensionalized by  $U_{\infty}$ ; time t was nondimensionalized by  $c/U_{\infty}$ ; pressure p and surface stress imposed on the fluid by the body f were nondimensionalized by  $\rho_f U_{\infty}^2$ , where  $\rho_f$  is the fluid density; g is the non-dimensional gravitational field using a reference g. The equation of motion of the torsional flap  $\Gamma_f$  is given by Eq. (4) where  $\chi_f$  is the Lagrangian coordinate

of  $\Gamma_f$ . The first term on the right hand side of Eq. (4) represents the moment about the hinge,  $\chi_f^0$ , due to the surface stress imposed on the fluid by the flap (thereby resulting in a negative sign). The second term represents the moment about  $\chi_f^0$  due to the gravitational force acting at the centre of gravity of the flap,  $\chi_f^{cg}$ . Note that, in this term, the mass of the flap is represented using the moment of inertia of the flap about the hinge. The no-slip boundary constraints on the airfoil and flap are given by Eq. (5) and (6), respectively. Here,  $\hat{e}^i$  is a unit vector denoting the direction of the angular velocity of the flap and  $\chi_a$  is the Lagrangian coordinate of the airfoil. These no-slip constraints are used to solve for the surface stress term  $f(\chi)$  that enforces the boundary condition that must hold on the respective bodies.

The flow equations (2)–(3) are spatially discretized using the standard second-order finite difference method and rewritten in a streamfunction-vorticity formulation. For time-discretization, Eq. (2) utilizes an Adams-Bashforth scheme for the nonlinear term and a Crank-Nicolson method for the diffusive term. The equation of motion of the flap (4) is discretized using an implicit Newmark scheme. The boundary condition constraints (5)–(6) and the surface stress term in Eq. (2) are evaluated implicitly at the current time step to enable stability of the method for flaps with a wide range of inertia and stiffness. The resulting fully discretized system of equations are subjected to a block-LU decomposition and iterated using Newton's method until convergence for the flap deflection angle. A multi-domain approach for treating far-field Dirichlet boundary conditions of zero vorticity is incorporated for solving the flow equations where a hierarchy of grids of increasing coarseness stretching to the far field is employed (see reference [23] for details).

Initially, the flap is rested at an angle of 5° from the airfoil surface, which is taken as the undeformed (zero stress) deflection angle. As the vortex shedding process occurs at the high angle of attack of 20°, the flap passively deploys and interacts with the flow. A grid-convergence study for a similar passively deployable airfoil-flap system, but with a NACA0012 airfoil was performed in Nair and Goza [21]. The converged grid parameters obtained from that convergence study are used in this work consisting of a NACA2414 airfoil. Accordingly, the spatial grid and time step sizes are set to be  $\Delta x/c = 0.00349$  and  $\Delta t/(c/U_{\infty}) = 0.0004375$ , respectively. Following Goza and Colonius [22], the immersed boundary spacing is set to be twice as that of the flow grid spacing of the finest grid. The convergence criteria for the fluid-structure coupling equation (not shown here; see reference [21]) is  $\|\Delta\beta\|_{\infty} \le 10^{-7}$ . A multi-domain approach is used for treating far-field boundary conditions with five grids of increasing coarseness, where the finest and coarsest grid levels are  $[-0.5, 2.5]c \times [-1.5, 1.5]c$  and  $[-23, 25]c \times [-24, 24]c$ , respectively.

### C. Experimental setup

### 1. Wind-tunnel setup

The experiments are conducted in a constant pressure, closed section, open-loop wind tunnel located in Talbot Laboratory at the University of Illinois at Urbana-Champaign. The wind tunnel has four test sections of increasing areas to minimize the streamwise pressure gradient [24]. The wing is mounted horizontally in the first test section closest to the inlet since it has the lowest turbulence level. The test section width is 90 cm and its height is 45 cm. One end of the wing section is mounted to the side of wind tunnel, while the other side is attached to a splitter plate to achieve 2D test conditions as shown in Fig. 4. The splitter plate allows the test section height to remain 45 cm while reducing the width to 28 cm, thereby minimizing the effects of the upper and lower section walls on the streamlines[16]. The forces on the wing are measured using an ATI Gamma 6- axis force/torque transducer which has a resolution of 1/60 N and a range of 0-32 N along with A B48 Velmex rotary table with a stepper motor to control the angle of the attack with a precision of 0.012°. The freestream velocity is measured using Omega volume flow anemometer placed upstream of the wing, between the splitter plate and the wind tunnel wall. The anemometer has a resolution of 0.01 m/s and an accuracy ±1.0% of reading. Furthermore, corrections are made in the post-processing code to account for solid and wake blockage and a velocity correction. [3, 25, 26].

The experiments are carried out at a free stream velocity of 26 m/s, which corresponds to  $Re = 2 \times 10^5$  and at  $\alpha = 20^\circ$ . The lift and drag forces are calculated from the measured forces, which were sampled at 1 kHz for 5 seconds. The flap dynamics including its flapping frequency and deflection angles are captured using Vision Research Phantom Miro eX4 Color high-speed camera at 600 fps. The flap footage were post processed using the ProAnalyst Motion Analysis Software.

### 2. Wing design

The wing section is fabricated using the Vero White material from an objet 260 connex3 3D printer. The hinge of the flap is designed such that there is two detachable circular hinges with a 2 mm diameter on each side of the wing that connects to similar circular hinges on the flap through a metal rod. The stiffness of the hinge is varied by inserting

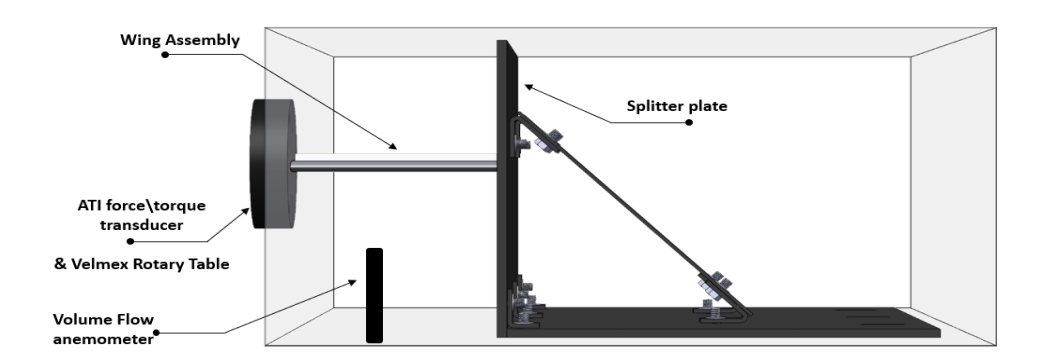
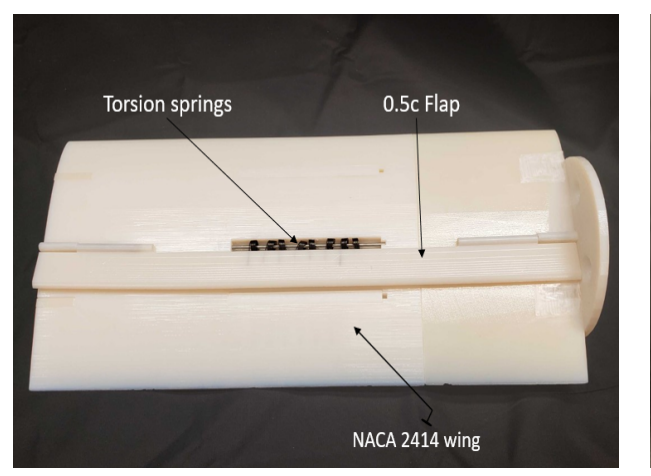
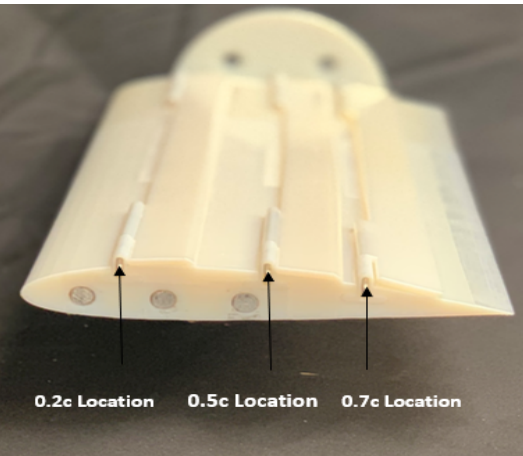


Fig. 4 Schematic of Wind tunnel setup and wing assembly

torsion springs around the metal rod, as shown in Fig. 5a. Each torsion spring has an outer diameter of 5.3 mm and a torsional stiffness of  $1.5 \times 10^{-3}$ N m/rad. We attach one, four, and eight springs in parallel to acquire dimensional torsional stiffness values of  $1.5 \times 10^{-3}$ ,  $6.0 \times 10^{-3}$ , and  $12 \times 10^{-3}$ N.m/rad, respectively. These dimensional stiffness values correspond to the non-dimensional stiffness values reported in Table 1. The flap inertia and mass are varied by selecting two different materials of different densities. More specifically, we used vero white and Mylar. These materials led to the following dimensional inertia values:  $8.53 \times 10^{-7}$  and  $8.64 \times 10^{-8}$ kg m<sup>2</sup>, respectively, also listed in Table 1 in their non-dimensional form.

The wing section design allows for changing the flap location. Fig. 5b shows the wing section with three flaps located at 0.2c, 0.5c, and 0.7c. During the experiments only one flap was tested, while the hinge locations for the other flaps were covered by 3D printed adaptors to maintain the airfoil profile. For example, Fig. 5a shows the wing section with a single flap placed at 0.5c and adaptors covering the other two flap location slots.





(a) NACA 2414 wing section with the 50% chord flap and eight (b) The wing section with three flaps located at 20% of torsional springs to achieve the highest stiffness value the chord, 50% of the chord, and 70% of the chord.

Fig. 5 NACA 2414 airfoil with flap and 8 torsional springs at 50% chord location (left) and showing the three tested flap hinge locations (right). During experiments, only a single flap is inserted while the other two flap locations are covered with adaptors to maintain the airfoil profile.

### III. Results

In this section, we show the results from the numerical simulations and the experimental study of the parameters detailed in Sec. II.A, including an in-depth discussion of the comparison between numerical simulations and experiments.

The mean quantities of lift and flap deflection reported in Sec. III.A are calculated once the airfoil-flap system reaches steady limit cycle oscillation, which corresponds to t > 25 for the simulations and at least 2 second ( $\approx 400c$ ) for the experiment.

# A. Effect of flap parameters on mean lift and flap deflection

#### 1. Numerical results at Re = 1000

A parametric study is performed to characterize the effect of varying flap parameters (i.e., flap stiffness, inertia, and location) on aerodynamic lift. The numerical results of this study for the parameters described in Table 1 are plotted in Fig. 6a–6c. In these plots,  $\Delta \overline{C}_l$  relative to the flap-less case in percentage is plotted against  $k_\beta$  for various  $i_\beta$ . It can be observed that significant lift improvements as high as  $\Delta \overline{C}_l = 12\%$  are attained for the flap located at 70% chord (Fig. 6c). While modest benefits of  $\Delta \overline{C}_l = 2\%$  are attained at the 20% location in Fig. 6a, and hardly any benefits are seen for the 50% case in Fig. 6b.

Across all the flap locations, the lift performance due to the lower inertia flaps are superior than the higher inertia flaps. This disparity is the largest for the flap at the 70% location in Fig. 6c, where flaps with a lower inertia of  $i_{\beta}=0.0012$  provided significant lift improvements while the flap with the larger inertia of  $i_{\beta}=0.012$  is detrimental to lift. For the cases providing appreciable lift benefits, such as the  $i_{\beta}=0.0012$  flaps at the 70% and 20% locations, highest performance is attained at the largest stiffness of  $k_{\beta}=0.001$ , with the lowest stiffness  $k_{\beta}=0.0001$  providing the least lift improvement.

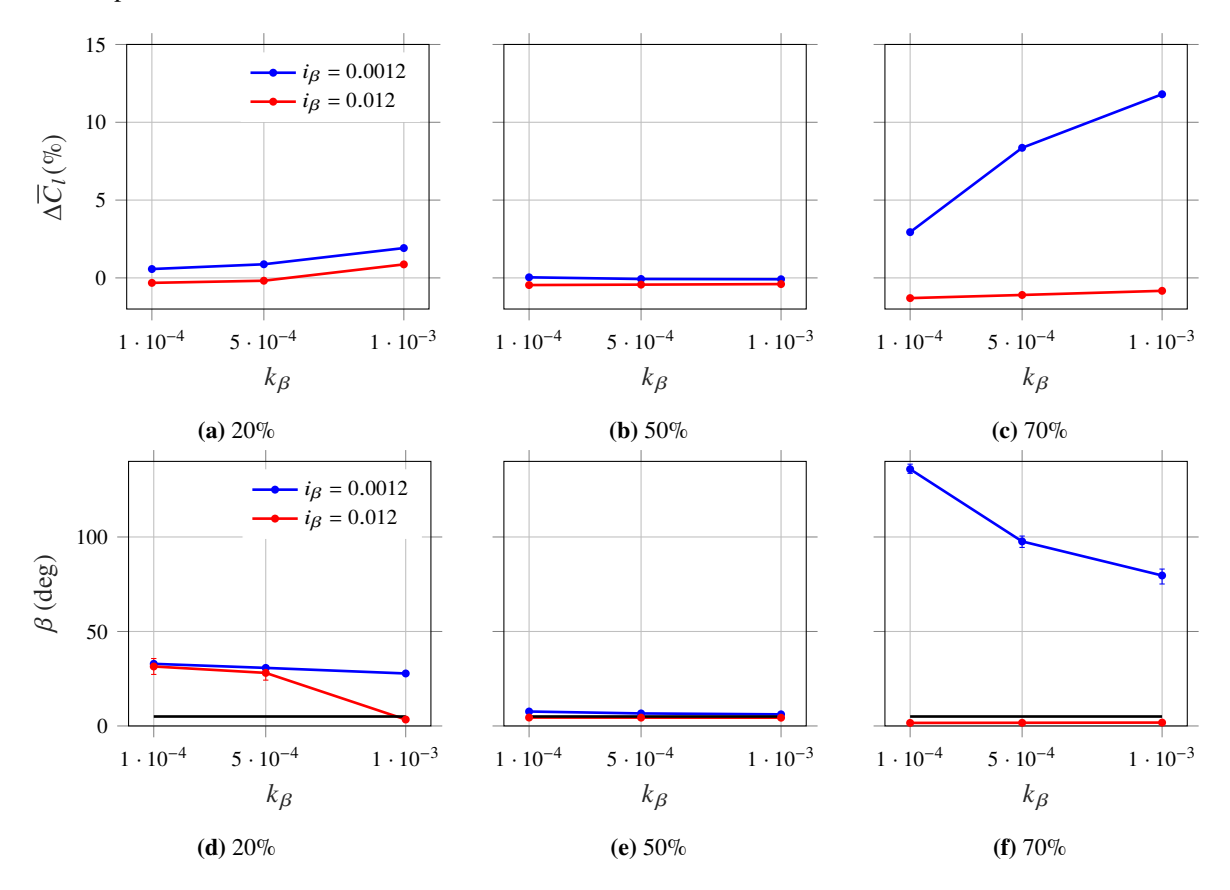


Fig. 6 Numerical results of the parametric study by varying stiffness and inertia for the flap mounted at 20%, 50% and 70% chord locations. The lift improvement of the airfoil as compared to the baseline flap-less case is plotted in the top row. Mean flap deflection and amplitude (denoted by vertical bars) is plotted in the bottom row.

To explain the effect of flap parameters on lift, we plot the mean flap deflection and amplitude of flap motion measured with respect to the airfoil surface in Fig. 6d–6f. In this plot, the markers denote the mean flap deflection angle,

 $\overline{\beta}$ , while the bars superimposed on these markers indicate the amplitude of flap oscillations. The black horizontal line at 5° denotes the initial flap deflection angle (as mentioned in Sec. II.B). A strong correlation between the flap deployments in Fig. 6d–6f and associated performance in Fig. 6a–6c can be deduced—the flaps with large mean deployment,  $\overline{\beta}$ , correspond to noticeable lift improvements while the flaps with negligible deployment do not provide any performance benefits. For instance, large flap deployments occur for flaps at 70% location in Fig. 6f, which also yield largest lift improvements in Fig. 6c. The moderate flap deployments at 20% location in Fig. 6d also result in noticeable lift benefits in Fig. 6a. On the other hand from Fig. 6e, the flaps at 50% location are hardly deployed and therefore, their associated benefits in Fig. 6b are negligible. It is also observed that generally, the larger inertia flaps have very low flap deployments (except for the 20% location in Fig. 6d), resulting in these cases being non-beneficial for lift as observed in the associated performance plots. The larger inertia flaps are not deployed because they are prone to larger gravitational forces by virtue of their mass. In fact, for some cases, the flap is pulled closer to the airfoil surface as compared to the initial deflection of 5° (c.f. Fig. 6f). These correlations between  $\overline{\beta}$  and  $\Delta \overline{C}_l$  clearly indicate that the passive deployment of the flap at post stall conditions is beneficial for aerodynamic lift.

We also observe that, as the stiffness is increased, the flap deployment angle decreases due to the increasing restoring torque imposed by the torsional spring. This phenomenon is more discernible at the 70% location in Fig. 6f. Here, we note that the mean flap deflection of  $\bar{\beta} \approx 80^{\circ}$  for the case of  $k_{\beta} = 0.001$  and  $i_{\beta} = 0.0012$  provides the most lift improvement. On the other hand, both the largest flap deflection (at  $k_{\beta} = 0.0001$ ,  $i_{\beta} = 0.0012$ ) and negligible flap deflection cases (at  $i_{\beta} = 0.012$ ) have reduced and insignificant aerodynamic benefits, respectively. Therefore, the mean deflection angle set by the combined effect of the aerodynamic forces of flow separation, restoring force due to  $k_{\beta}$  and gravitational force due to  $\bar{\beta}$  seems to play an important role in providing significant lift improvements.

# 2. Experimental results at $Re = 2 \times 10^5$

In this section, we show the experimental results at  $Re=2\times10^5$  for the three different stiffness cases and the three different inertia cases listed in Table 1 at the post stall angle of  $\alpha=20^\circ$ . Fig. 7a–7c shows  $\Delta \overline{C}_l$  percentage relative to the baseline flap-less case, and Fig. 7d–7f show mean flap deflection angle  $\overline{\beta}$  both plotted against the stiffness  $k_\beta$  for various inertia values  $i_\beta$  at the three tested locations. Firstly, we observe from Fig. 7a–7c that the flap with the lower inertia  $i_\beta=0.0012$  has higher  $\Delta \overline{C}_l$  percentage in comparison to the higher inertia flap  $i_\beta=0.012$  across all locations. The highest  $\Delta \overline{C}_l$  ( $\tilde{1}1\%$ ) is observed for the highest stiffness case of  $k_\beta=0.001$  and low inertia flap located at 70% location, while the high inertia flap at the same location has a max  $\Delta \overline{C}_l$  percentage around 6%. At the 50% flap location, the low inertia flap provides minimal lift improvements ( $\Delta \overline{C}_l \sim 2\%$ ), while the high inertia flap is detrimental to lift with ( $\Delta \overline{C}_l \sim -11\%$ ). At 20% location the flap doesn't show any significant lift improvements or detriments with a  $\Delta \overline{C}_l$  range between (-4%–2%).

Secondly, we analyze the mean flap deflection angle and amplitude of flap motion measured with respect to the airfoil surface in Fig. 7d–7f. In these plots, the markers denote the mean flap deflection angle,  $\overline{\beta}$ , while the bars superimposed on these markers indicate the amplitude of flap oscillations. First, we notice that the  $\overline{\beta}$  and the amplitude for the low inertia flap is higher than the high inertia flap since they experience lower gravitational forces due to their lower mass. The amplitude for the low inertia flap is an order of magnitude greater than the high inertia flap at all locations. Additionally, the mean deflection angle decreases almost linearly with the stiffness for the 50% and 70% chord locations due to the higher restoring torque imposed by the torsional spring; however, a different trend is observed at the 20% location, where the mean beta stays constant around 23° for the low inertia flap. This constant mean deployment angle suggests an accelerating flow above this angle which prevents the flap from deploying any more than this regardless of decreasing the stiffness. For the 70% location, as the stiffness increase the mean deflection angle decreases for both inertia cases. On the other hand, at the 70% location, the lift improvement  $\Delta \overline{C}_l$  percentage increases as the stiffness increase. The maximum lift improvement is 11% for the low inertia flap and 6% for the high inertia flap. These lift improvements correspond with a mean deflection angle of 12.5° and 8.7°, respectively.

# 3. Discussion of key similarities and differences between numerical and experimental parametric studies

Several similarities as well as differences between numerical and experimental results are identified and discussed here. Note that the numerical results for the larger mass flap of  $i_{\beta} = 0.012$  are not considered in the discussion. This is because the  $i_{\beta} = 0.012$  flap is hardly deployed since at low Re = 1,000, the gravitational forces act much more strongly on the flap than at the much larger  $Re = 2 \times 10^5$  experiments even though the Froude number for both simulations and experiments are held the same. Readers are referred to [27, 28] for a discussion on the effect of inertia on the flap and

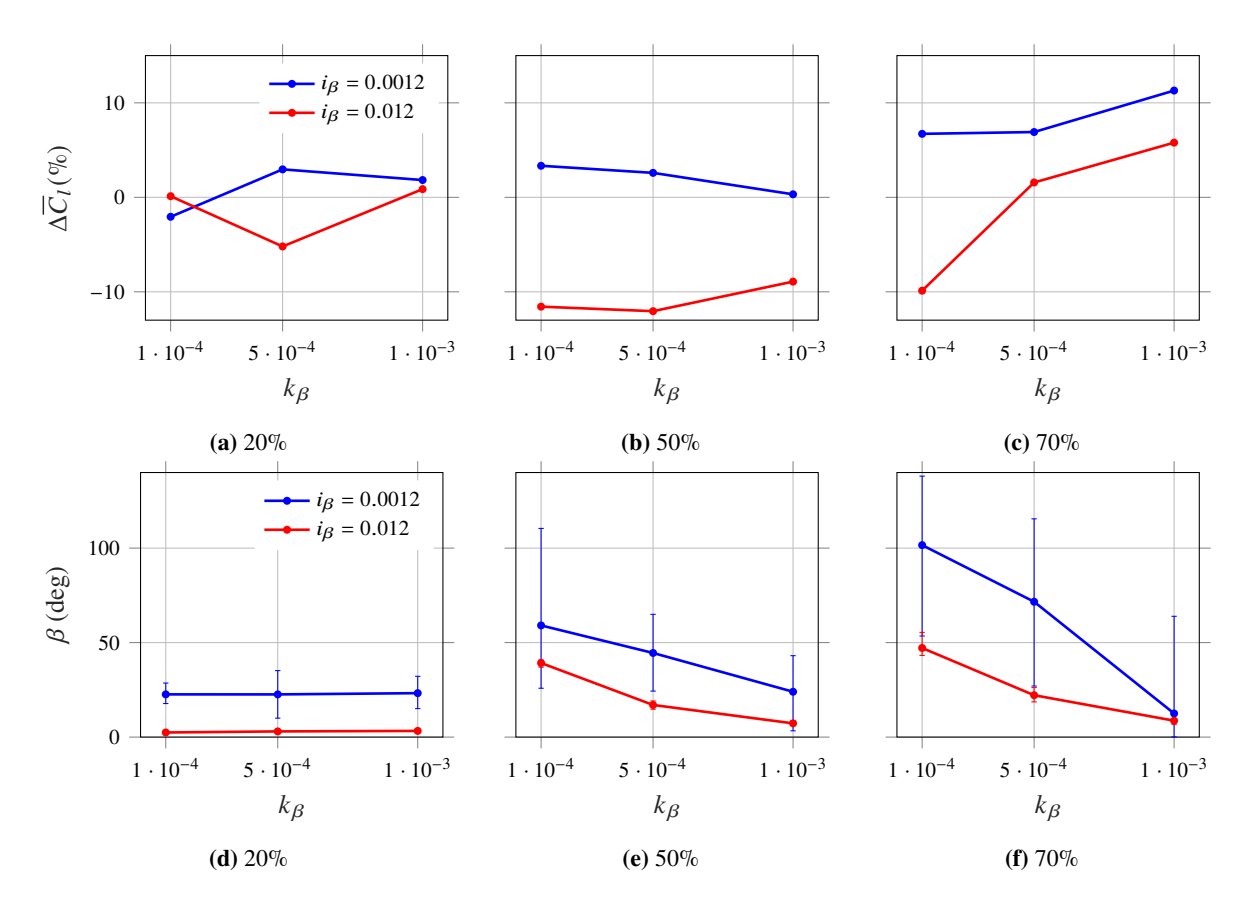


Fig. 7 Experimental results of the parametric study by varying stiffness and inertia for the flap mounted at 20%, 50% and 70% chord locations. The lift improvement of the airfoil as compared to the baseline flap-less case is plotted in the top row. Mean flap deflection and amplitude (denoted by vertical bars) is plotted in the bottom row.

lift dynamics in the absence of gravity at Re = 1,000.

One of the key similarities between simulations and experiments is observed at the 70% location case. Firstly, maximum lift across all flap parameters considered in this work is attained at 70% location,  $i_{\beta}=0.0012$  and  $k_{\beta}=0.001$  for both simulations (c.f. Fig. 6c) and experiments (c.f. Fig. 7c). Moreover, the magnitudes of lift improvement for both are also similar at  $\Delta \overline{C}_{l} \approx 12\%$ . Besides the maximal case, the qualitative trend of increasing lift performance with increasing stiffness is exhibited in both results. The trends of mean flap deployment in Fig. 6f and Fig. 7f also exhibit key similarities in the sense that (a) flaps at 70% chord deploy the most as compared to the 20% and 50% locations and (b)  $\overline{\beta}$  decreases with increasing stiffness due to increasing restoring forces of the spring. While we have seen in Sec. III.A.2 that the amplitude of flap oscillations decreases with increasing inertia for experiments, it is also true for simulations, albeit in the absence of gravity as described in [28]. These similarities in large lift improvements and similar flap deployment trends may be owed to significant vortex shedding commonly occurring in both simulations and experiments at the post-stall angle of attack of  $\alpha=20^{\circ}$ , whose effect is more pronounced downstream, for example, at the 70% location.

The parametric results at the upstream location of 20% largely exhibit similarities barring some qualitative differences. For instance, the peak lift improvement at this location is  $\Delta \overline{C}_l \approx 2-3\%$  for both simulations (c.f. Fig. 6a) and experiments (c.f. Fig. 7a). However, the stiffness values where the maximal lift is attained are different at  $k_\beta = 0.001$  and  $k_\beta = 0.0005$  for simulations and experiments, respectively. In contrast to the qualitative differences in the  $\Delta \overline{C}_l$  trends, a key similarity is found in the mean flap deployment angle. It can be seen that for  $i_\beta = 0.0012$ , the mean flap deployment relatively remains constant across stiffness values that are an order of magnitude apart, albeit at distinct  $\overline{\beta} \approx 30^\circ$  (c.f. Fig. 6d) and  $\overline{\beta} \approx 20^\circ$  (c.f. Fig. 7d) for simulations and experiments, respectively. Since at post-stall angles of attack, flow separates at a relatively upstream location, we hypothesize that the similarities observed at 20% location may be owed to laminar

flow separation near the leading edge resulting in similar flap interactions with the separated shear layer.

Finally, in contrast to the similarities observed at the 70% and 20% locations, significant differences between simulations and experiments are observed at the 50% location. Firstly, no lift benefits are attained at Re = 1,000 (c.f. Fig. 6b), while experiments at  $Re = 2 \times 10^5$  yield  $\Delta \overline{C}_l \approx 3\%$  (c.f. Fig. 7b). This is because the flap in the simulations are hardly deployed (c.f. Fig. 6f) in contrast to considerable  $\overline{\beta}$  observed in experiments in Fig. 7f. We hypothesize that the lack of flap deployment and interactions with the separated flow may be due to its mid-chord location where it is unable to interact with either the vortex shedding process occurring downstream (like in the 70% case) or the laminar separated shear layer originating upstream (like in the 20% case). In contrast, at  $Re = 2 \times 10^5$  in experiments, turbulence related smaller scale structures and disturbances might be aiding the passive deployment of the flap which provides lift improvements. Therefore, the differences at the 50% location may be owed to the differences in the laminar and turbulent behavior in simulations and experiments, respectively.

## B. Effect of flap parameters on lift and flap deflection dynamics

### 1. Numerical results at Re = 1000

To understand how the flap affects the flow-field and airfoil lift dynamics and how the vortex shedding process in turn affects the flap dynamics, we have plotted  $\beta(t)$  and  $C_I(t)$  for the case the produces the best lift improvement, namely at 70% location,  $i_{\beta} = 0.0012$ ,  $k_{\beta} = 0.001$  (Fig. 8). From Fig. 8a, we can see that the flap is initially undeployed at t = 0. As the flow separation and vortex shedding process occurs, the flap deploys at  $t \approx 3$  eventually reaching a steady limit cycle oscillation (LCO) regime where the flap oscillates about a mean deflection angle with constant amplitude. Similar LCO behavior is observed for the lift dynamics in Fig. 8b for both the flap and flap-less cases.

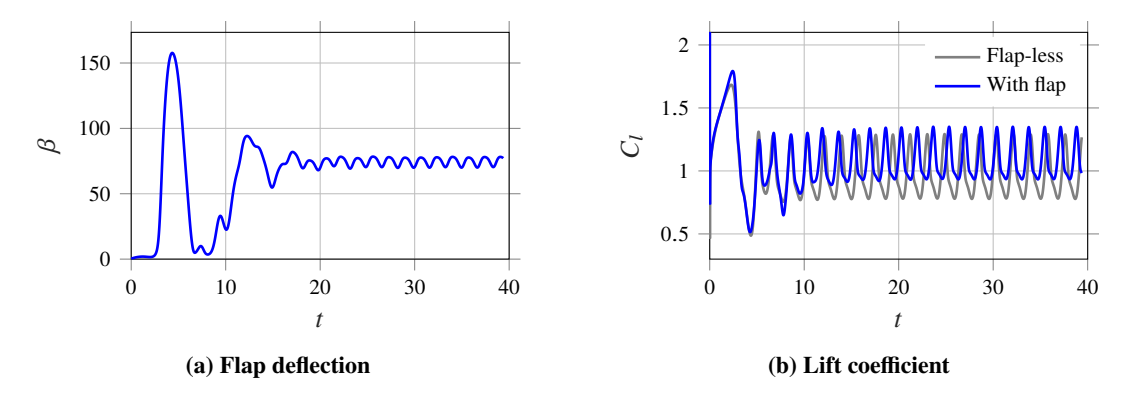


Fig. 8 Plots of flap deflection,  $\beta$ , and lift coefficient,  $C_l$ , for the flap-less case and the case of flap hinge located at 70%,  $k_{\beta} = 0.001$  and  $i_{\beta} = 0.0012$  obtained from numerical simulations.

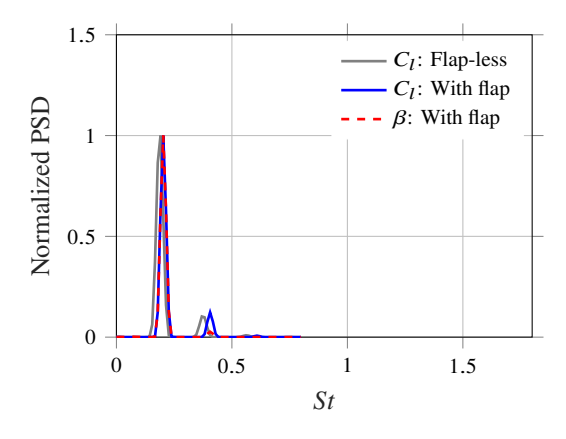


Fig. 9 Normalized power spectral density (PSD) of the lift and flap deflection signals in Fig. 8 for the flap-less case and the case of flap hinge located at 70%,  $k_{\beta} = 0.001$  and  $i_{\beta} = 0.0012$  obtained from numerical simulations.

For each of these temporal plots, the normalized power spectral density is plotted in Fig. 9. Here the x-axis represents the Strouhal number defined as  $St = fc \sin(\alpha)/U_{\infty}$ , where the length scale  $c \sin(\alpha)$  is the projected chord length normal to the flow direction.  $St \approx 0.2$  is observed to be the dominant frequency for all the lift and flap dynamics. This frequency corresponds to the frequency of vortex shedding. Moreover, the vortex shedding frequency stays the same for both the flap-less and the flapped cases. Furthermore, the flap oscillates at the same frequency as that of vortex shedding, instead of its natural frequency. Therefore, the airfoil-flap system represents a forced vibration system with the aerodynamic forces of vortex shedding being the time varying external forcing.

## 2. Experimental results at $Re = 2 \times 10^5$

In this section, the experimental temporal plots of both  $\beta(t)$  and  $C_l(t)$  for the case with the greatest lift improvement  $(\Delta \overline{C}_l = 12\%)$  corresponding to the flap with  $i_\beta = 0.0012$  and  $k_\beta = 0.001$  at 70% flap location is shown in Fig. 10. In these two figures, time is non-dimensionalised by the free stream velocity over the chord (Convection time  $t = timexU_\infty/c$ ). We see that the flap shifts the lift signal up, increasing the value of its mean compared to the baseline, and the flap deflection angle oscillates around 10°. However, we see some unsteady behavior where some peak angles appear between 40° and 60°. For each of these temporal plots, the normalized power spectral density is plotted in Fig. 11, where the x-axis represents the Strouhal number defined as  $St = fc\sin(\alpha)/U_\infty$ ,  $St \approx 0.27$  is observed to be the dominant frequency for both the flap-less baseline and the flapped cases which corresponds to the frequency of vortex shedding. The presence of the flap doesn't seem to alter the vortex shedding frequency of the original system, rather it just influences the mean. As for the flap deflection angle, multiple frequencies appear. Such wide spectrum might be an indication of the various turbulence scales that are affecting the flap deflection at  $Re = 2 \times 10^5$ . Nevertheless, a significant peak appears at  $St \approx 0.27$  as well, which corresponds to the vortex shedding frequency.

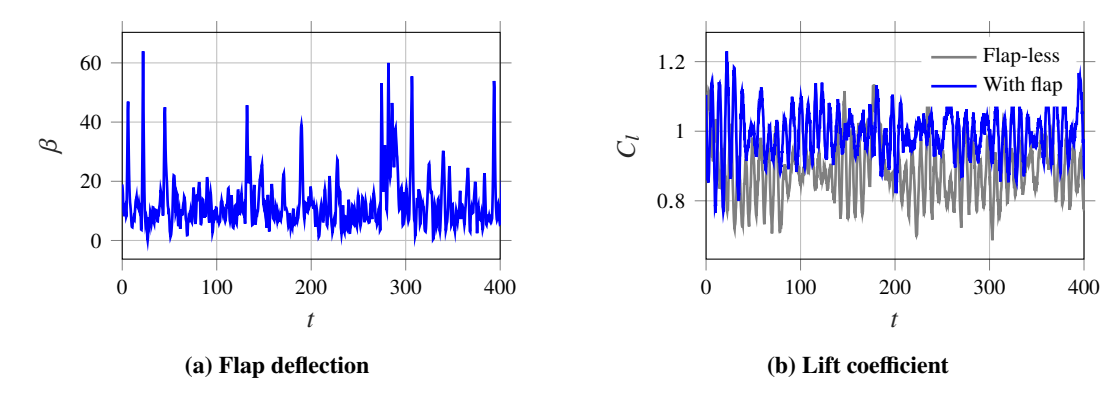


Fig. 10 Plots of flap deflection,  $\beta$ , and lift coefficient,  $C_l$ , for the flap-less case and the case of flap hinge located at 70%,  $k_{\beta} = 0.001$  and  $i_{\beta} = 0.0012$  obtained from experiments.

### 3. Discussion of key similarities and differences between numerical and experimental lift and flap dynamics

In this section, the key similarities and differences in the lift and flap dynamics between the low Re numerical study and high Re experiment are discussed. For this comparison, we focus on the case with the highest  $\Delta \overline{C}_l$ , attained at 70% location,  $i_{\beta} = 0.0012$  and  $k_{\beta} = 0.001$  for both the low Re simulations and high Re experiments. First, we notice that the shedding frequency for the flap configuration is the same as the flap-less case for both the numerical simulation ( $St \approx 0.20$ ) and the experiment ( $St \approx 0.27$ ) as shown in Fig. 9 and Fig.11, respectively. This indicates that the flap doesn't alter the shedding frequency of the airfoil for either Reynolds numbers. Furthermore, this vortex shedding frequency appears in the power spectrum plot for the flap oscillation in both the experiment and the simulation.

There are also some observable difference in the flap and lift dynamics between simulation and experiments. The flap deflection angle of the experimental study doesn't reach a fully steady limit cycle oscillation like the numerical low Re study; instead, intermittent peaks are observed for the experimental flap deflection angle as shown in Fig. 10a. Moreover, in the simulations, only one dominant frequency is evident in the flap oscillation spectrum, and this frequency corresponds to the shedding frequency. However, for the high Re experiment, the flap oscillations have a broad spectrum with multiple frequencies apparent (Fig. 11b), rather than one clear dominant frequency. Such wide spectrum is indicative of the turbulent flow and scales affecting surrounding the flap at this Reynolds number.

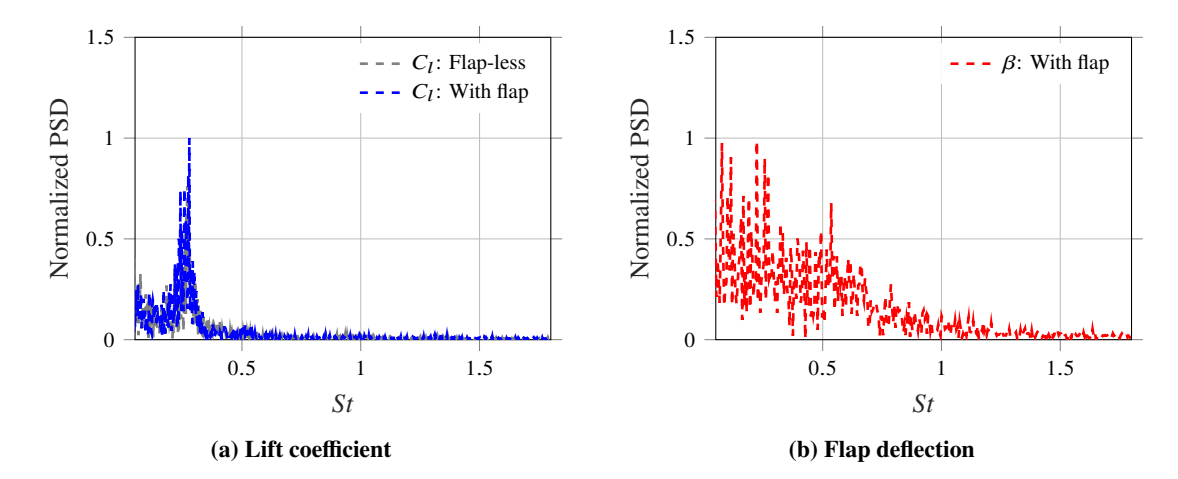


Fig. 11 Normalized power spectral density (PSD) of the lift and flap deflection signals in Fig. 8 for the flap-less case and the case of flap hinge located at 70%,  $k_{\beta} = 0.001$  and  $i_{\beta} = 0.0012$  obtained from experiments.

### C. Qualitative flow features for the numerical low Re case

In this section, we qualitatively analyze the lift enhancing flow structures that are modulated by the flap dynamics at Re = 1000. In Fig. 12, we have plotted the vorticity contours in one time period of the lift cycle in the steady LCO regime for the highest lift improvement case of  $i_{\beta} = 0.0012$ ,  $k_{\beta} = 0.001$  and 70% location. Here, a lift cycle is defined between two consecutive peaks of  $C_l$ . The periodic formation, shedding and interaction of the leading (LEV) and trailing (TEV) edge vortices can be clearly observed from these plots. The time instants of t/T = 0 and t/T = 0.55 approximately correspond to the instants of maximum LEV and TEV strengths, where T is the time period of the lift cycle. Similar vortex shedding is observed for the flap-less case and plotted in Fig. 13. On comparing the streamlines of the flap and flap-less cases of Fig. 12 and 13 respectively, we can observe that the flap is able to block the reverse flow induced by flow separation, specifically by the TEV in Fig. 12b and 12c, as compared to that of the flap-less case in Fig. 13b and 13c. This blocking of the upstream propagation of reverse flow is hypothesized to be the dominant contributor to the observed lift improvements.

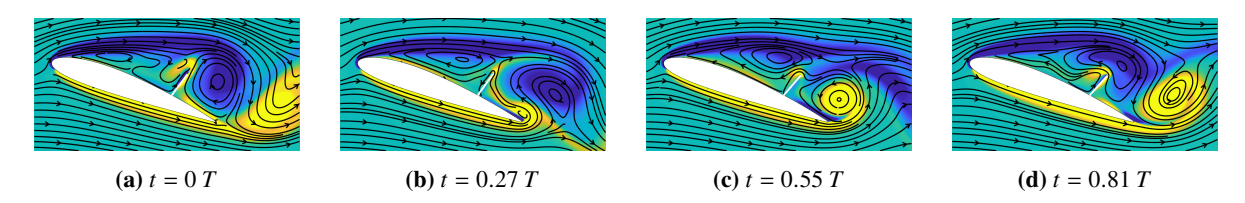


Fig. 12 Vorticity contours at different time instants in one period of lift cycle for the case of flap hinge located at 70% of the chord length from the leading edge,  $k_{\beta} = 0.001$  and  $i_{\beta} = 0.0012$ .

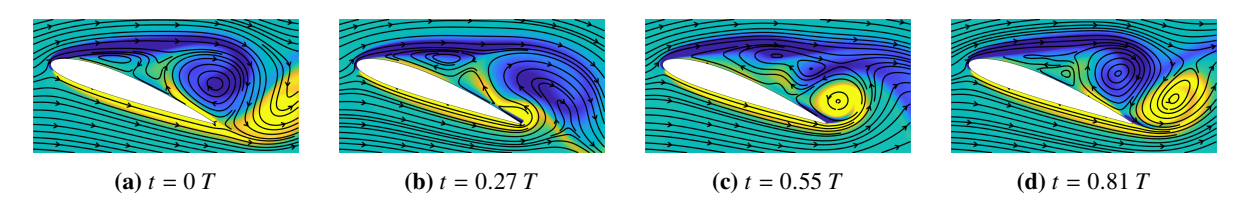


Fig. 13 Vorticity contours at different time instants in one period of lift cycle for the flap-less case.

### IV. Conclusions and Future Work

In this manuscript, we investigated the fluid-structure interaction and aerodynamic effects of a passively deployable, torsionally hinged covert-inspired flap mounted on the suction side of an airfoil at two different Reynolds numbers, numerically at Re = 1000 and experimentally at  $Re = 2 \times 10^5$ . The analysis was conducted at a post-stall angle of attack of 20° at both Re, where significant flow separation and vortex shedding occur. First, a parametric study was performed by varying the flap location, inertia, and stiffness. At both Re numerically and experimentally, the flap was found to be effective at improving lift post-stall. Lift improvements as high as 12% with respect to the baseline flap-less airfoil were achieved at the low inertia flap with the highest stiffness located at the 70% location in both the simulation and the experiment. Furthermore, the parametric study showed a lot of similarities for the location near the LE or TE (20% and 70% locations), especially the low inertia flaps, which are the cases that show the most lift benefits occur. However, the 50% location is where large disparities appeared due to the different flow inertia at the two Re. Moreover, it was observed that the mean deflection angle can be controlled by changing the stiffness at the location near the trailing edge for the low inertia flap at both Re; however, near the leading edge, the deployment angle stays constant, regardless of the stiffness. Next, we examined the lift and the flap dynamics for the case with the highest lift improvement to understand the mechanism by which the flap improves lift. The flap and Lift dynamics were found to be comparable at both Re; however, unsteadiness is evident at the higher Re regime due to turbulence effects. For instance, the vortex shedding frequency was found to remain the same between the baseline flap-less case and the flapped case, and the flap was found to oscillate at the same frequency as the vortex shedding frequency at both Re. However, the flow unsteadiness at the high Re results in a wider frequency spectrum for the flap oscillations compared to the low Re case. Finally, by investigating the vorticity contour of the highest lift improvement case of the numerical simulation, it was observed that the flap blocks the reverse flow induced by flow separation, specifically by the trailing edge vortices. This blocking of the upstream propagation of reverse flow is hypothesized to be the dominant contributor to the observed lift improvements. In this study, similarities were found for the FSI dynamics and associated lift generating mechanisms at both the numerical low Re case and the experimental high Re case. This means that for this system, low Re simulations can be performed to help inform and design the experiment at higher Re since fully resolved numerical models are prohibitively costly for those. Future work would involve studying the effect of multiple torsionally hinged covert-inspired flaps with particle image velocimetry (PIV) to reveal the true physical insight and flow characteristics of the covert inspired flow control technique, especially at high Re. Future work could also include studying the influence of the covert-inspired flap on dynamic pitching of an airfoil to inform more realistic models for the landing and perching dynamics of birds.

### V. Acknowledgments

This work was funded by the National Science Foundation's engineering directorate (Award Number: 2029028).

### References

- [1] Anderson, J. D., John D., Fundamentals of aerodynamics, 3<sup>rd</sup> ed., McGraw-Hill series in aeronautical and aerospace engineering, McGraw-Hill, Boston, 2001.
- [2] Morris, I., Wallace J., and Rusak, Z., "Stall onset on aerofoils at low to moderately high Reynolds number flows." *Journal of Fluid Mechanics*, Vol. 733, 2013, p. 439.
- [3] Selig, M., Broeren, A. P., and Giguère, P., Summary of low-speed airfoil data: low-speed airfoil test, University of Illinois at Urbana-Champaign, SoarTech, Virginia Beach, Va, 1995.
- [4] Abbott, I. H. A., *Theory of wing sections, including a summary of airfoil data*, [corrected version / with a new pref. by the authors]. ed., Dover Publications, New York, 1959.
- [5] Kroo, P. J. K. I. M., "Analysis, Design, and Testing of Airfoils for Use at Ultra-Low Reynolds Numbers," 2004.
- [6] Rose, J. B. R., Natarajan, S. G., and Gopinathan, V. T., "Biomimetic flow control techniques for aerospace applications: a comprehensive review." *Reviews in Environmental Science & Biotechnology*, Vol. 20, No. 3, 2021, pp. 645 677.
- [7] Ito, M. R., Duan, C., Chamorro, L. P., and Wissa, A. A., "A leading-edge alula-inspired device (LEAD) for stall mitigation and lift enhancement for low Reynolds number finite wings," *ASME 2018 Conference on Smart Materials, Adaptive Structures and Intelligent Systems*, American Society of Mechanical Engineers Digital Collection, 2018.

- [8] Lee, K. J., and Wissa, A., "Dynamic characterization of a bio-inspired variable stiffness multi-winglet device," *Behavior and Mechanics of Multifunctional Materials IX*, Vol. 11377, edited by R. L. Harne, International Society for Optics and Photonics, SPIE, 2020, pp. 57 66. https://doi.org/10.1117/12.2558348, URL https://doi.org/10.1117/12.2558348.
- [9] Carruthers, A., Thomas, A., and Taylor, G., "Automatic aeroelastic devices in the wings of a steppe eagle Aquila nipalensis." *Journal of Experimental Biology*, Vol. 210, No. 23, 2007, pp. 4136–4149.
- [10] Bachmann, T., Emmerlich, J., Baumgartner, W., Schneider, J. M., and Wagner, H., "Flexural stiffness of feather shafts: geometry rules over material properties," *Journal of Experimental Biology*, Vol. 215, No. 3, 2012, pp. 405–415. https://doi.org/10.1242/jeb.059451, URL https://doi.org/10.1242/jeb.059451.
- [11] Proctor, N., and Lynch, P., *Manual of Ornithology: Avian Structure & Function*, Yale University Press, 1993. URL https://books.google.com/books?id=nQ3vLQkEWQMC.
- [12] Bechert, D., Bruse, M., Hage, W., Meyer, R., Bechert, D., Bruse, M., Hage, W., and Meyer, R., "Biological surfaces and their technological application-laboratory and flight experiments on drag reduction and separation control," 28th Fluid dynamics conference, 1997, p. 1960.
- [13] Altman, A., and Allemand, G., "Post-stall performance improvement through bio-inspired passive covert feathers," 54th AIAA Aerospace Sciences Meeting, 2016, p. 2042.
- [14] Brücker, C., and Weidner, C., "Influence of self-adaptive hairy flaps on the stall delay of an airfoil in ramp-up motion," *Journal of Fluids and Structures*, Vol. 47, 2014, pp. 31–40.
- [15] Rosti, M. E., Omidyeganeh, M., and Pinelli, A., "Passive control of the flow around unsteady aerofoils using a self-activated deployable flap," *Journal of Turbulence*, Vol. 19, No. 3, 2018, pp. 204–228.
- [16] Duan, C., and Wissa, A., "Covert-inspired flaps for lift enhancement and stall mitigation." Bioinspiration & biomimetics, Vol. 16, No. 4, 2021.
- [17] Meyer, R., Hage, W., Bechert, D. W., Schatz, M., Knacke, T., and Thiele, F., "Separation Control by Self-Activated Movable Flaps," *AIAA journal*, Vol. 45, No. 1, 2007, pp. 191–199.
- [18] Pixabay/TheOtherKev, 2021. URL https://pixabay.com/photos/heron-in-flight-blue-heron-heron-4158846/.
- [19] Atlas, U. F. W. S. F., 2021. URL https://www.fws.gov/lab/featheratlas/feather.php?Bird=GBHE\_covert\_imm.
- [20] Wang, L., Alam, M. M., and Zhou, Y., "Experimental study of a passive control of airfoil lift using bioinspired feather flap," *Bioinspiration & biomimetics*, Vol. 14, No. 6, 2019, p. 066005.
- [21] Nair, N. J., and Goza, A., "A strongly coupled immersed boundary method for fluid-structure interaction that mimics the efficiency of stationary body methods," *arXiv preprint arXiv:2103.06415*, 2021.
- [22] Goza, A., and Colonius, T., "A strongly-coupled immersed-boundary formulation for thin elastic structures," *Journal of Computational Physics*, Vol. 336, 2017, pp. 401–411.
- [23] Colonius, T., and Taira, K., "A fast immersed boundary method using a nullspace approach and multi-domain far-field boundary conditions," Computer Methods in Applied Mechanics and Engineering, Vol. 197, No. 25-28, 2008, pp. 2131–2146.
- [24] Ito, M. R., Duan, C., and Wissa, A. A., "The function of the alula on engineered wings: a detailed experimental investigation of a bioinspired leading-edge device," *Bioinspiration & biomimetics*, Vol. 14, No. 5, 2019, p. 056015.
- [25] Barlow, J., Rae, W., and Pope, A., Low-Speed Wind Tunnel Testing, John Wiley & Sons, Canada, 1999.
- [26] Apelt, C., and West, G., "The Effects of Wake Splitter Plates on Bluff-Body Flow in the Range 104< R< 5× 104. Part 2," *Journal of Fluid Mechanics*, Vol. 71, No. 1, 1975, pp. 145–160.
- [27] Nair, N. J., and Goza, A., "Effects of Torsional Stiffness and Inertia on a Passively Deployable Flap for Aerodynamic Lift Enhancement," AIAA SCITECH 2022 Forum, 2022, p. 1968.
- [28] Nair, N. J., and Goza, A., "Fluid-structure interaction of a bio-inspired passively deployable flap for lift enhancement," *arXiv* preprint arXiv:2203.00037, 2022.